

MAGNETIZED MOVING MESH MERGER OF A CARBON-OXYGEN WHITE DWARF BINARY

CHENCHONG ZHU, RÜDIGER PAKMOR, MARTEN H. VAN KERKWIJK, PHILIP CHANG

(Dated: December 3, 2024)
Draft version December 3, 2024

ABSTRACT

White dwarf binary mergers are possible progenitors to a number of unusual stars and transient phenomena, including type Ia supernovae. To date, simulations of mergers have not included magnetic fields, even though they are believed to play a significant role in the evolution of the merger remnant. We simulated a 0.625 - 0.65 M_{\odot} carbon-oxygen white dwarf binary merger in the magnetohydrodynamic moving mesh code AREPO. Each white dwarf was given an initial dipole field with a surface value of $\sim 10^3$ G. As in simulations of merging double neutron star binaries, we find exponential field growth within Kelvin-Helmholtz instability-generated vortices during the coalescence of the two stars. The final field has complex geometry, and a strength $> 10^{10}$ G at the center of the merger remnant. Its energy is $\sim 2 \times 10^{47}$ ergs, $\sim 0.2\%$ of the remnant's total energy. The strong field likely influences further evolution of the merger remnant by providing a mechanism for angular momentum transfer and additional heating, potentially helping to ignite carbon fusion.

Key words: *binaries: close – white dwarfs – hydrodynamics – supernovae: general*

1. INTRODUCTION

White dwarf (WD) binaries are common end products of binary stellar evolution. Gravitational wave emission, magnetic braking or the influence of a third body will cause a fraction of these to merge, producing a diversity of unusual stars and electromagnetic transients. In particular, for double carbon-oxygen (CO) WD mergers, the final outcome could be a massive and rapidly-rotating WD (eg. Segretain et al. 1997), an accretion-induced collapse into a neutron star (Saio & Nomoto 1985), or a nuclear explosion that might resemble a type Ia supernova (SN Ia). Understanding the conditions that lead to each outcome depends on understanding the merging process, which has been investigated with increasingly sophisticated 3D hydrodynamic simulations since the pioneering study of Benz et al. (1990). More recent work has focused on precise binary initial conditions (Dan et al. 2011), merger properties across the WD binary parameter space (eg. Zhu et al. 2013; Dan et al. 2014), and under what conditions nuclear reactions become important during the merger (eg. Dan et al. 2012; Moll et al. 2014). However, one fundamental piece missing in WD merger studies so far is magnetic fields.

Mergers (that do not immediately explode) are expected to produce differentially rotating merged objects - “merger remnants” - that are susceptible to magnetic dynamo processes such as the magnetorotational instability (MRI; Balbus & Hawley 1991), Tayler-Spruit dynamo (eg. Spruit 2002), and the $\alpha\omega$ dynamo (if convection occurs in the inner disk; García-Berro et al. 2012). It has therefore long been suspected that they can generate strong fields, and recent 2D simulations of MRI in the remnant (Ji et al. 2013) have indeed shown amplification of a weak seed field to $> 10^{10}$ G. Magnetic shear from these fields transports angular momentum over a timescale of $\sim 10^4 - 10^8$ s (van Kerkwijk et al. 2010; Shen et al. 2012) – far shorter than the thermal timescale of the remnant – and also (non-locally) heats the remnant. The latter, combined with loss of rotational support from angular momentum transport, could push remnant temperatures past the point of carbon ignition ($\sim 6 \times 10^8$ K for densities be-

tween $10^5 - 10^7$ g cm⁻³), leading to either stable nuclear burning or a runaway. This mechanism could potentially drive nuclear runaways even in remnants with masses below the Chandrasekhar Mass M_{Ch} that have traditionally been considered stable (van Kerkwijk et al. 2010).

While field growth after the merger has been explored, field growth *during* the merger is also expected, and can have a profound impact on the post-merger magnetic evolution. Magnetohydrodynamic (MHD) double neutron star (NS) binary merger simulations (eg. Price & Rosswog 2006; Kiuchi et al. 2014; Giacomazzo et al. 2014) have found that Kelvin-Helmholtz vortices produced along the shear interface between the coalescing stars can amplify field strengths by orders of magnitude (Obergaullinger et al. 2010; Zrake & MacFadyen 2013). The same should hold true for WD mergers. Motivated by this, we present the first MHD simulation of a sub- M_{Ch} 0.625 - 0.65 M_{\odot} CO WD binary merger.

2. METHODS

We employ the moving-mesh code AREPO (Springel 2010), which solves the equations of ideal MHD on a Voronoi mesh coupled with self-gravity. We operate the code in its pseudo-Lagrangian mode, so that the mesh-generating points that define the Voronoi grid move with the local velocity of the fluid. To conserve angular momentum to within $\sim 2\%$ of its initial value, we use the latest improvements to time integration and gradient estimate (Pakmor et al. 2015). AREPO's MHD implementation is described in Pakmor et al. (2011) and Pakmor & Springel (2013); we use the Powell et al. (1999) eight-wave scheme for divergence control.

We model the merger of two carbon-oxygen WDs with masses of 0.625 and 0.65 M_{\odot} , respectively, in a circular, unsynchronized binary with initial separation $a_0 = 2.20 \times 10^9$ cm (corresponding period $P_0 = 49.5$ s) chosen according to Eggleton (1983). Our initial conditions are very similar to those of the 0.625 - 0.65 M_{\odot} binary simulated with smoothed-particle hydrodynamics (SPH) in Zhu et al. (2013; henceforth Z13). As in Z13, we chose masses typical of the narrowly-peaked empirical mass distribution of field CO WDs (Tremblay & Bergeron 2009). Both WDs are generated with a uniform initial temperature of 5×10^6 K and a uniform composition

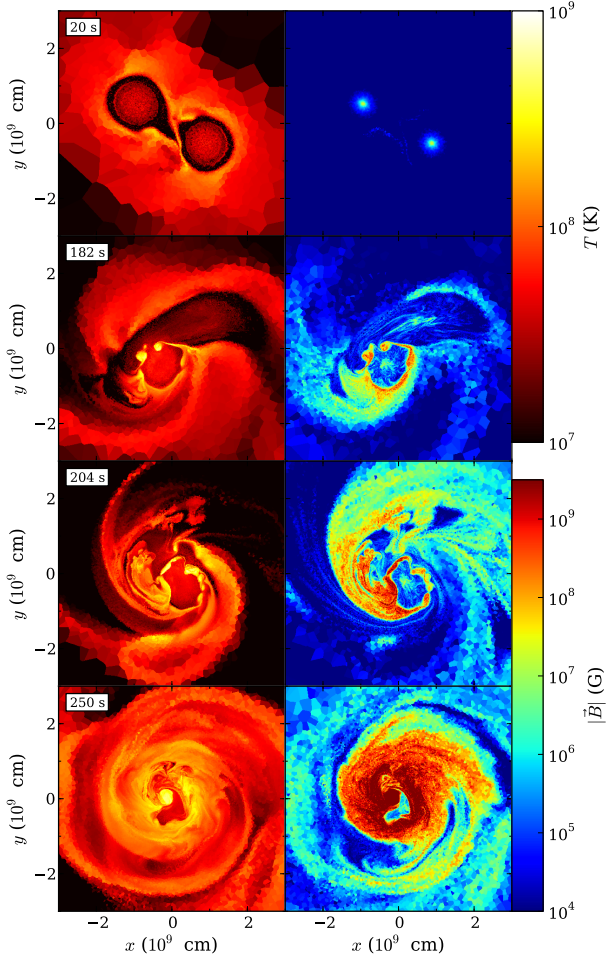


Figure 1. Series of temperature T (left column) and magnetic field strength $|\vec{B}|$ (right) logarithmic intensity profiles in the equatorial plane of the merger for four snapshots in time (rows; time indicated at the top left of each row).

of equal parts carbon and oxygen by mass. They are separately relaxed to hydrostatic equilibrium using the SPH code GASOLINE (Wadsley et al. 2004) and added to AREPO by converting the SPH particles to mesh-generating points while retaining their conservative quantities (mass, momentum and energy). A uniform $10^{-5} \text{ g cm}^{-3}$ background grid fills up a 10^{12} cm box centered on the binary. Each WD is given a (dynamically irrelevant) dipole seed magnetic field with an equatorial surface value of 10^3 G (and corresponding central field of $\sim 2 \times 10^7 \text{ G}$). The fields are overlapped when the two stars are placed into a binary.

The mass resolution of our simulation is $m_{\text{cell}} \approx 1 \times 10^{-6} M_{\odot}$. We utilize explicit refinement and derefinement (Vogelsberger et al. 2012) to keep cell masses within a factor of two of $10^{-6} M_{\odot}$ and to ensure adjacent cells differ by less than a factor of 10 in volume.

3. RESULTS

We depict the evolution of the binary in Fig. 1, highlighting temperature T and magnetic field strength $|\vec{B}|$. Fig. 2 shows the growth of total magnetic energy E_B over time.

In the first stage of the merger, up to $\sim 180 \text{ s}$, the 0.625

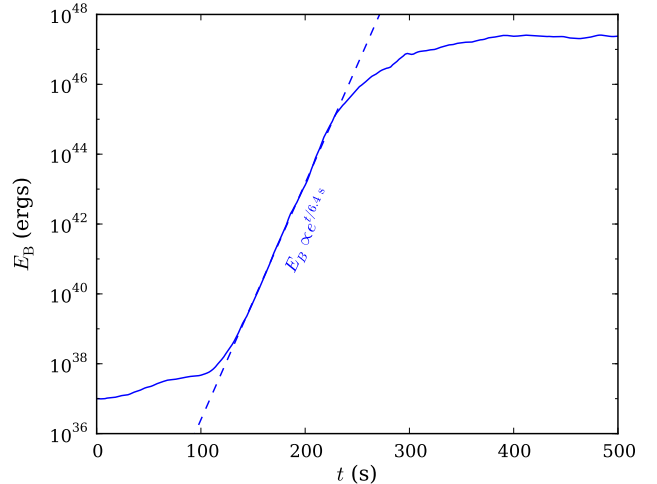


Figure 2. Total magnetic energy E_B over time, with a best fit to the rapid exponential growth (dashed $E_B \propto e^{t/6.4s}$ line).

M_{\odot} donor WD transfers mass to the $0.65 M_{\odot}$ accretor for about 3.5 orbits before fully disrupting. Because our initial conditions are approximate – the WDs are not initially tidally deformed – mass transfer begins in spurts as the WDs stretch in response to the binary potential, and occurs at a rate that is artificially high (Dan et al. 2011). The early mass transfer shears the atmospheres of both WDs. As a result, E_B grows roughly linearly in the first $\sim 100 \text{ s}$, reaching about quadruple its initial value. Since the initial mass transfer rate is artificially high, this growth is likely an overestimate, but remains negligible compared to what follows.

By $\sim 120 \text{ s}$, mass transfer becomes steady, and a stream of material from the donor wraps around the accretor, forming a shear layer. Along it, the Kelvin-Helmholtz instability generates a string of hot vortices that exponentially amplify their entrained magnetic fields. This is illustrated in Fig. 1 (row 2), where the hot vortices along the donor-accretor interface correspond to regions of high field strength. At $\sim 180 \text{ s}$, tidal forces between the two WDs become strong enough to fully disrupt the donor, which then coalesces with the accretor over $\sim 50 \text{ s}$. During this time, infalling donor material spirals into the accretor, severely deforming the accretor while carrying the string of magnetized vortices toward the system’s center of mass (CM). Fig. 2 shows E_B growing exponentially by a factor of $\sim 10^7$ over $\sim 100 \text{ s}$, with an e-folding time $\tau = 6.4 \text{ s}$, comparable to the typical turnover timescale of the largest eddies $2\pi R_{\text{eddy}}/\Delta v_{\text{shear}} \sim 3 \text{ s}$, where Δv_{shear} is the velocity difference across the shear layer.

By $\sim 250 \text{ s}$ many of the vortices have merged together into a hot, rapidly rotating underdense void at the CM (Fig. 1, row 4). Magnetic growth within the void begins to saturate as its magnetic and kinetic energy approach equipartition. The rate of field growth slows as well, with E_B growing another two orders of magnitude over $\sim 150 \text{ s}$ before plateauing at $\sim 2 \times 10^{47} \text{ ergs}$ at $\sim 400 \text{ s}$.

In Fig. 3 we show the density ρ , T , $|\vec{B}|$ and ratio of magnetic to rotational energy density e_B/e_{rot} of the merger remnant at 400 s . The remnant consists of a dense, degeneracy-supported core containing $\sim 60\%$ of the remnant’s mass, a partly thermally-supported hot envelope that surrounds the core, and a rotationally-supported disk, a configuration similar to the SPH $0.625\text{-}0.65 M_{\odot}$ remnant from Z13. The AREPO

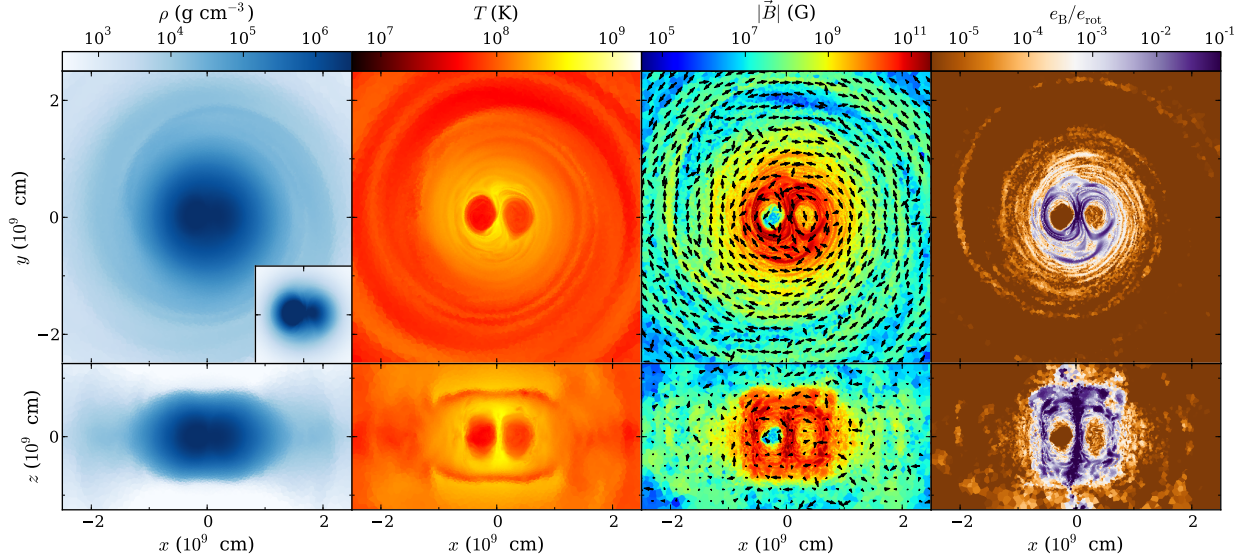


Figure 3. From leftmost to rightmost column, equatorial plane (top row) and polar (bottom) logarithmic intensity profiles of density ρ , temperature T , magnetic field strength $|\vec{B}|$ and ratio of magnetic to rotational energy density e_B/e_{rot} for the simulation at 400 s (~ 170 s after coalescence). The equatorial plane density plot includes a linear profile (with the same x and y scale as the logarithmic profile) of the remnant core to show its shape. Arrows in the magnetic field strength plots indicate field directions, with their lengths equal to the fraction of the field that lies along the xy plane (top frame) and xz plane (bottom).

remnant core, however, has distinctly non-axisymmetric density and temperature structures, unlike the SPH simulation which achieves axisymmetry ~ 150 s after coalescence (Z13, Fig. 2). The magnetic fields are too weak during the merger to have an effect on the merger dynamics, so these contrasts are due to differences in the *hydrodynamic* schemes between AREPO and SPH (Zhu et al., in prep.).

The remnant magnetic field configuration is complex: while field lines are coherent along “strands” of high field strength, neighbouring strands often point in opposite directions (see Fig. 3). In the core, the volume-averaged field strength is 4×10^{10} G, but strands of $> 10^{11}$ G field perforate the core. The field remains $> 10^9$ G near the core-disk interface at $\sim 10^9$ cm, before dropping below 10^7 G at $\gtrsim 3 \times 10^9$ cm. The total magnetic field energy is $\sim 0.2\%$ the total, $\sim 0.6\%$ the total rotational, and $\sim 6\%$ the total differential rotation energy of the remnant.¹ This energy is roughly equally partitioned into toroidal and poloidal field components, with the ratio of poloidal to total magnetic energy $E_{B,\phi}/E_B = 0.62$. Studies of local field amplification within Kelvin-Helmholtz vortices predict magnetic growth saturates when the magnetic and kinetic energy densities are close to equipartition (Obergaullinger et al. 2010; Zrake & MacFadyen 2013). In our simulation, this is only the case for the strands of $> 10^{11}$ G, where magnetic energy density is $\sim 7\%$ ($\sim 47\%$) the rotational (differential rotation) energy density (see Fig. 3, column 4). It is possible that because the strands are distributed throughout the core, they drive the core’s overall evolution and inhibit further magnetic amplification in their surroundings.

Some of the magnetized accretion stream is ejected during coalescence and integrates into the inner disk ($\sim 1 - 3 \times 10^9$ cm), producing a $10^7 - 10^8$ G field by 400 s. This field has a negligible hydrodynamic effect on the disk (magnetic energy

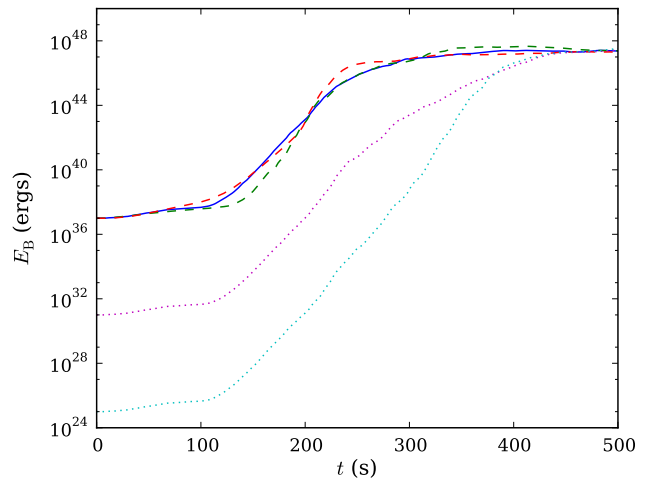


Figure 4. Total magnetic energy E_B over time for the fiducial (solid blue; $m_{\text{cell}} \approx 1 \times 10^{-6} M_{\odot}$, equatorial surface field strength $\sim 10^3$ G) simulation and the robustness tests. Dashed lines represent low (green; $m_{\text{cell}} \approx 5 \times 10^{-6} M_{\odot}$) and high resolution (red; $m_{\text{cell}} \approx 2 \times 10^{-7} M_{\odot}$) simulations. Dotted lines represent ~ 1 G (magenta) and $\sim 10^{-3}$ G (cyan) low initial field simulations.

density to pressure ratio $e_B/P \approx 3 \times 10^{-5}$ at 2×10^9 cm), and, unlike the field in the core, has *not* saturated: $|\vec{B}|$ continues to grow exponentially with $\tau \sim 200$ s.²

4. ROBUSTNESS TESTS

4.1. Resolution Test

To check that our results are not resolution-limited, we performed simulations, otherwise identical to the fiducial one in Sec. 3, with lower and higher mass resolutions of $m_{\text{cell}} \approx$

¹ Differential rotation energy of a cell is estimated with $E_{\text{drot}} = m_{\text{cell}} |\vec{v}| |\nabla \times \vec{v}| V_{\text{cell}}^{1/3}$.

² The remnant disk is generally poorly resolved, even at the highest resolution used in Sec. 4.1; this may artificially slow the disk field growth rate.

$5 \times 10^{-6} M_{\odot}$ and $m_{\text{cell}} \approx 2 \times 10^{-7} M_{\odot}$, respectively. Fig. 4 compares the E_B evolution between these simulations (dashed lines) and the fiducial one (solid).

The three runs are qualitatively identical. Donor disruption and the start of exponential field growth occurs ~ 0.75 orbital periods earlier at low resolution, and ~ 0.5 periods later at high, because the outer layers of the WDs are better captured, and the differences in hydrostatic equilibrium between AREPO and GASOLINE less pronounced, at higher resolution. Exponential growth rates are similar between the runs - the E_B e-folding time during exponential growth is $\tau = 4.9$ s for the low resolution run, faster than $\tau = 6.4$ s for the fiducial. At high resolution, the growth curve appears to be separated into two phases, with $\tau = 7.8$ s before coalescence, and $\tau = 3.9$ s during it. The total magnetic energy at the end of exponential growth is also similar - at 400 s, E_B is $\sim 4 \times 10^{47}$ ergs in the low resolution run and $\sim 1.5 \times 10^{47}$ ergs in the high, compared to $\sim 2 \times 10^{47}$ ergs at the fiducial resolution. The fiducial and high resolution runs also qualitatively have very similar magnetic field structures by 400 s. Our fiducial resolution of $1 \times 10^{-6} M_{\odot}$ therefore appears sufficient for qualitatively capturing the growth and final field configuration of the merger.

In their MHD disk galaxy simulations, Pakmor & Springel (2013) find faster field growth and higher field strength at saturation in their lowest resolution run, which they attribute to larger divergence errors at lower resolution. We perform a similar test, and also see a trend of decreasing divergence error (and more accurate magnetic evolution) at higher resolution, though the errors of all our simulations are at least a factor of two smaller than any reported in Pakmor & Springel (2013). The errors are highly localized in space and trace steep magnetic gradients, suggesting they contribute only to small-scale variations in the magnetic field.

4.2. Changing the Seed Field Strength

To understand the dependence of our results on the initial seed field, we ran two additional simulations in which we decreased the strength of the seed field by 3 and 6 orders of magnitude leading to an initial equatorial surface field of 1 G (central field $\sim 2 \times 10^4$ G), and $\sim 10^{-3}$ G (~ 20 G), respectively. We plot their E_B evolution (dotted lines) in Fig. 4. We find the growth curves to be homologous between both low initial field runs and the fiducial one - differing only by the ratios of seed E_B - up to ~ 200 s, with the e-folding time for exponential amplification approximately 6.5 s for all three runs. By ~ 250 s, the field in the fiducial simulation begins to plateau, while amplification (of initially weaker fields) continues for several hundred more seconds in the low initial field runs. For both runs, E_B plateaus at $\sim 3 \times 10^{47}$ ergs, comparable to the fiducial $\sim 2 \times 10^{47}$ ergs. Because the fields in the low initial field runs remain dynamically irrelevant for longer, however, their structures differ from that of the fiducial run and resemble more the crescent in Fig. 1, row 4. The disk field does not saturate in any simulation - its strength is proportional to the strength of the seed field, and is thus much weaker in the low initial field runs. Our tests thus suggest that the exponential growth, growth timescale and plateau E_B are robust to changes in initial field strength, while the remnant field configuration is more sensitive to the choice of seed field.

5. DISCUSSION

We have shown that the merger of a $0.625 - 0.65 M_{\odot}$ CO WD binary produces a strong, $> 10^{10}$ G magnetic field with a complex structure that winds through the remnant core and into the inner disk. Similar to previous simulations of binary NS mergers, the strong field is generated by dynamo action within Kelvin-Helmholtz vortices formed during the coalescence of the two WDs. Since these vortices are ubiquitous in WD mergers, strong magnetic fields are a likely feature of all merger remnants. The degree to which a field permeates the remnant core depends on how thoroughly the donor and accretor mix during coalescence, which itself is sensitive to initial conditions such as the degree of synchronization between the WDs, or how accurately their tidal bulges and early mass transfer are captured (Dan et al. 2011, 2014). A parameter space study of magnetized mergers is needed to investigate the range of possible remnant field configurations.

We note that NS mergers simulated in Eulerian grid codes generally show E_B growing by only a factor of $\sim 10^2 - 10^3$ during coalescence, compared to the $\sim 10^9$ we see, despite these simulations having resolutions comparable or superior to our low resolution AREPO run. This weaker growth is also inconsistent with the amplification to local kinetic equipartition seen in small-scale simulations (Obergaullinger et al. 2010; Zrake & MacFadyen 2013), and is attributed to insufficient resolution in the NS merger simulations (Kiuchi et al. 2014; Giacomazzo et al. 2014, though see Dionysopoulou et al. 2015). Giacomazzo et al. (2014) incorporated a sub-grid magnetic amplification model, calibrated using Zrake & MacFadyen (2013)'s results, into their Eulerian NS merger simulation, and found E_B amplification by a factor of $\sim 10^{10}$ over a single dynamical time.³ This suggests AREPO may be better able to resolve small-scale velocity structures than an Eulerian code at comparable resolution, or better able to couple these structures to magnetic growth. Further work is needed to understand the magnetic field growth in detail.

The density profile of the remnant remains non-axisymmetric for hundreds of seconds after coalescence. As a result, the core continues to evolve dynamically, and by 400 s has begun to launch a pair of spiral waves into the surrounding medium (see the density panel of Fig. 3), which transport angular momentum on a timescale rivaling that for magnetic shear. While Kashyap et al. (2015) report a similar spiral instability in their Eulerian remnant evolution simulation, SPH simulations like those of Z13 rapidly achieve axisymmetry after coalescence and do not form spiral waves. As noted earlier, this difference between AREPO and SPH simulations is a product of the differences between their hydrodynamic schemes. Further study is needed to understand these differences and their consequences for remnant evolution (Zhu et al., in prep.).

The post-merger evolution of the remnant has been followed to $\sim 10^4$ s with axisymmetric cylindrical (two-dimensional) Eulerian grid simulations (Schwab et al. 2012; Ji et al. 2013). As described earlier, Ji et al. (2013)'s MHD simulation of a $0.6 - 0.6 M_{\odot}$ remnant shows the development of a strong magnetic field due to MRI. The subsequent heating and angular momentum transport due to the fields pushes core temperatures to ignition, supporting the possibility of a nuclear runaway within sub- M_{Ch} remnants. Their re-

³ Price & Rosswog (2006)'s SPH simulations also show strong amplification; while runs using their Euler potential MHD method suffer exaggerated field growth from improper boundary conditions, their \vec{B} -based runs show similar results (Price 2012).

sults are, however, likely sensitive both to their initial hydrodynamic conditions – which may have artificially high core temperatures – and their chosen seed magnetic field, a pure poloidal one to optimize the onset of MRI. Our much stronger poloidal-toroidal field could substantially change post-merger evolution. Moreover, the persistence of a non-axisymmetric remnant core will lead to evolution that clearly cannot be captured in an axisymmetric cylindrical grid. We therefore stress the need to perform high-resolution three-dimensional simulations of post-merger evolution to determine the final fate of the remnant.

There are a number of potentially observable consequences of the magnetic fields produced by the merger. Ji et al. (2013) note the creation of a magnetized corona and biconal jet in their simulations, which act in concert to cause an outflow of material near the remnant’s poles. This outflow eventually unbinds $\sim 10^{-3} M_{\odot}$ of material, and Beloborodov (2014) estimates it should lead to an optical transient with a duration of ~ 1 day and peak $L \sim 10^8 L_{\odot}$, which should be detectable by optical surveys.

If a remnant later experiences a nuclear runaway and explodes as a SN Ia, its magnetic field will increase the late-time emission by trapping positrons (produced by ^{56}Co β^+ decay) that would otherwise escape the ejecta. The trapping efficiency depends on the strength and configuration of the remnant magnetic field, with a locally entangled $\sim 10^{11}$ G field – similar to our findings – well able to trap positrons past 1000 days (Ruiz-Lapuente & Spruit 1998). This is in line with observed late-time SN Ia light curves (most recently Kerzendorf et al. 2014).

Those remnants that do not explode will retain strong fields when they reach quiescence, and populate the high-mass tail of the distribution of isolated high-field magnetic white dwarfs (HFWDs; García-Berro et al. 2012; Külebi et al. 2013; Wickramasinghe et al. 2014; Briggs et al. 2015). Their properties might be akin to the recently-discovered hot DQ WDs (eg. Dufour et al. 2013; Williams et al. 2013; Lawrie et al. 2013), which have carbon-dominated atmospheres and $T_{\text{eff}} \approx 2 \times 10^4$ K, are often strongly magnetized (~ 1 MG) and sometimes have monophasic photometric variability (possibly due to rapid rotation). If most known hot DQs are massive ($M \gtrsim 0.95 M_{\odot}$), the population’s velocity dispersion corresponds to a kinematic age much older than what would be inferred from their temperatures, suggesting that hot DQs are WD-WD merger remnants instead of single star evolutionary products (Dunlap & Clemens, in press). Their observed properties would then constrain merger and remnant evolutionary models, and double-degenerate channels for SNe Ia.

We thank Christopher Thompson, Christopher Matzner, Volker Springel, Bart Dunlap, Yuri Levin, Henk Spruit, Ue-Li Pen and Stephen Ro for their insight into magnetohydrodynamics and simulations. This work utilized the SciNet HPC Consortium’s GPC supercomputer (Loken et al. 2010). CZ acknowledges support from the Natural Sciences and Engi-

neering Research Council (NSERC) Vanier Canada Graduate Scholarship. RP acknowledges support by the European Research Council under ERC-StG grant EXAGAL-308037 and by the Klaus Tschira Foundation. PC is supported by the NASA ATP program through NASA grant NNX13AH43G, and NSF grant AST-1255469.

REFERENCES

- Balbus, S. A. & Hawley, J. F. 1991, *ApJ*, 376, 214
 Beloborodov, A. M. 2014, *MNRAS*, 438, 169
 Benz, W., Cameron, A. G. W., Press, W. H., & Bowers, R. L. 1990, *ApJ*, 348, 647
 Briggs, G. P., Ferrario, L., Tout, C. A., Wickramasinghe, D. T., & Hurley, J. R. 2015, *MNRAS*, 447, 1713
 Dan, M., Rosswog, S., Brüggén, M., & Podsiadlowski, P. 2014, *MNRAS*, 438, 14
 Dan, M., Rosswog, S., Guillochon, J., & Ramirez-Ruiz, E. 2011, *ApJ*, 737, 89
 —. 2012, *MNRAS*, 422, 2417
 Dionysopoulou, K., Alic, D., & Rezzolla, L. 2015, arXiv:1502.02021
 Dufour, P., Vornanen, T., Bergeron, P., & Fontaine, A., B. 2013, in *Astronomical Society of the Pacific Conference Series*, Vol. 469, 18th European White Dwarf Workshop., ed. Krzesiński, J. ski, G. Stachowski, P. Moskalik, & K. Bajan, 167
 Eggleton, P. P. 1983, *ApJ*, 268, 368
 García-Berro, E. et al. 2012, *ApJ*, 749, 25
 Giacomazzo, B., Zrake, J., Duffell, P., MacFadyen, A. I., & Perna, R. 2014, arXiv:1410.0013
 Ji, S. et al. 2013, *ApJ*, 773, 136
 Kashyap, R., Fisher, R., García-Berro, E., Aznar-Siguán, G., Ji, S., & Lorén-Aguilar, P. 2015, *ApJ*, 800, L7
 Kerzendorf, W. E., Taubenberger, S., Seitzzahl, I. R., & Ruitter, A. J. 2014, *ApJ*, 796, L26
 Kiuchi, K., Kyutoku, K., Sekiguchi, Y., Shibata, M., & Wada, T. 2014, *Phys. Rev. D*, 90, 041502
 Külebi, B., Ekşi, K. Y., Lorén-Aguilar, P., Isern, J., & García-Berro, E. 2013, *MNRAS*, 431, 2778
 Lawrie, K. A., Burleigh, M. R., Dufour, P., & Hodgkin, S. T. 2013, *MNRAS*, 433, 1599
 Loken, C. et al. 2010, *Journal of Physics Conference Series*, 256, 012026
 Moll, R., Raskin, C., Kasen, D., & Woosley, S. E. 2014, *ApJ*, 785, 105
 Obergaulinger, M., Aloy, M. A., & Müller, E. 2010, *A&A*, 515, A30
 Pakmor, R., Bauer, A., & Springel, V. 2011, *MNRAS*, 418, 1392
 Pakmor, R. & Springel, V. 2013, *MNRAS*, 432, 176
 Pakmor, R. et al. 2015, arXiv:1503.00562
 Powell, K. G., Roe, P. L., Linde, T. J., Gombosi, T. I., & De Zeeuw, D. L. 1999, *Journal of Computational Physics*, 154, 284
 Price, D. J. 2012, *Journal of Computational Physics*, 231, 759
 Price, D. J. & Rosswog, S. 2006, *Science*, 312, 719
 Ruiz-Lapuente, P. & Spruit, H. C. 1998, *ApJ*, 500, 360
 Saio, H. & Nomoto, K. 1985, *A&A*, 150, L21
 Schwab, J., Shen, K. J., Quataert, E., Dan, M., & Rosswog, S. 2012, *MNRAS*, 427, 190
 Segretain, L., Chabrier, G., & Mochkovitch, R. 1997, *ApJ*, 481, 355
 Shen, K. J., Bildsten, L., Kasen, D., & Quataert, E. 2012, *ApJ*, 748, 35
 Springel, V. 2010, *MNRAS*, 401, 791
 Spruit, H. C. 2002, *A&A*, 381, 923
 Tremblay, P.-E. & Bergeron, P. 2009, *ApJ*, 696, 1755
 van Kerkwijk, M. H., Chang, P., & Justham, S. 2010, *ApJ*, 722, L157
 Vogelsberger, M., Sijacki, D., Kereš, D., Springel, V., & Hernquist, L. 2012, *MNRAS*, 425, 3024
 Wadsley, J. W., Stadel, J., & Quinn, T. 2004, *New Astr.*, 9, 137
 Wickramasinghe, D. T., Tout, C. A., & Ferrario, L. 2014, *MNRAS*, 437, 675
 Williams, K. A. et al. 2013, *ApJ*, 769, 123
 Zhu, C., Chang, P., van Kerkwijk, M. H., & Wadsley, J. 2013, *ApJ*, 767, 164
 Zrake, J. & MacFadyen, A. I. 2013, *ApJ*, 769, L29